PHYSICAL REVIEW B **101**, 155201 (2020)

Establishing best practices to model the electronic structure of $CuFeO_2$ from first principles

Matteo Ferri,[1,2] Joshua Elliott,[2,*] Stefano Fabris,[2] and Simone Piccinin[2,†]
[1]*International School for Advanced Studies (SISSA), Via Bonomea 265, 34136 Trieste, Italy*
[2]*CNR-IOM, Consiglio Nazionale delle Ricerche–Istituto Officina dei Materiali, c/o SISSA, Via Bonomea 265, 34136 Trieste, Italy*

(Received 16 December 2019; revised manuscript received 10 February 2020; accepted 18 March 2020; published 10 April 2020)

The cuprous delafossite, $CuFeO_2$, has received significant attention in recent years as a potential photocathode material in photoelectrochemical water-splitting cells. Presented herein is an investigation of the electronic structure of $CuFeO_2$ in the framework of density functional theory. We have benchmarked three of the most popular formulations for the treatment of the electron exchange and correlation interactions, highlighting their strengths and weaknesses in predicting electronic structures compatible with the available spectroscopic measurements. Although some features are correctly reproduced by the simplest approach, which is based on the generalized gradient approximation, this fails in describing the fundamental semiconducting character of the material. The introduction of the fully self-consistent Hubbard U correction in the exchange correlation functional accounts explicitly for the on-site Coulomb interaction among localized d electrons, thereby opening a gap in the band structure. However, our results indicate that the U correction disrupts the crystal-field splitting of the t_{2g} and e_g states, resulting in an inaccurate description of the conduction-band edge. We provide a qualitative and quantitative analysis to explain why the t_{2g} and e_g states behave differently when the Hubbard correction is switched on. We find that best practice for accurate, yet computationally viable, simulations of CFO makes use of hybrid functionals, where the fraction of exact exchange is not arbitrarily selected but tuned according to the static dielectric constant of the material. In this case, theoretical predictions are found to be in excellent agreement with experimental results.

DOI: 10.1103/PhysRevB.101.155201

I. INTRODUCTION

Tandem photoelectrochemical (PEC) solar cells, composed of two different photoactive electrodes, target higher photoconversion efficiencies than single-adsorber cells through independent optimization of the anode and cathode [1,2]. In this setup, the ideal cathodic material provides photogenerated electrons at the semiconductor-electrolyte interface, driving the H_2 evolution reaction (HER). Due to its visible light band gap and first optical transition, and the ideal energetic alignment of its conduction-band edge for electron transfer in the HER, cuprous oxide (Cu_2O) has attracted considerable interest as the photocathode in PEC water-splitting cells [3–5]. Yet, its performance is limited by several drawbacks. The most critical drawback is that Cu_2O exhibits poor stability in water, which not only makes it necessary to apply a surface protective layer [6], but also increases the cost and complexity of the photocathode engineering, thus limiting large-scale industrial production.

Leveraging the advantages of Cu_2O, Cu(I)-based ternary compounds have subsequently been suggested as alternative candidates in the role of photocathode [7–9]. Among them, the delafossite phase of $CuFeO_2$ (CFO) stands out, with particularly favorable properties for the HER [7,10–13]. At low temperature, CFO exhibits different phases, which were previously investigated for their multiferroic effects [14–17]. Delafossite CFO can harvest a large portion of the solar spectrum, with an optical band gap of around 1.5 eV [10,13,18], and like Cu_2O, its conduction-band minimum (CBM) is also in a favorable position to drive the cathodic reaction. Importantly, where Cu_2O degrades, CFO benefits from stability in aqueous environments, thereby removing the need for protective layers. In addition, CFO offers a practical advantage in that it is composed of cheap, earth abundant elements that can be combined in facile synthesis. Several different strategies for the growth of CFO crystals have been reported, including electrodeposition [7], pulsed laser deposition [19], sol-gel synthesis [10], and reactive cosputtering [13].

However, in spite of the encouraging favorable properties, the photocurrent measured in the bare CFO electrode is lower than expected [10]. It is speculated that this is in part due to poor bulk electron-hole separation, possibly induced by long-lived excited states [13], and due to the presence of surface states [12] that act as traps, favoring the electron-hole recombination. It has been shown that the low photocurrent is enhanced by surface functionalization with an electron scavenging molecule [10], and by creating heterojunctions between CFO and other compounds, for example $CuAlO_2$ [11,20] or CuO [21,22]. These heterojunctions separate the photogenerated electron and hole pairs, increasing the overall performance of the electrode.

---

[*] Present address: Department of Chemical Engineering and Analytical Science, University of Manchester, Manchester M13 9PL, United Kingdom.

[†] piccinin@iom.cnr.it

The electronic structure of CFO has been well characterized experimentally. The first x-ray photoemission experiments aimed at investigating the valence manifold were carried out by Galakhov *et al.* [23]. A comparison of the Cu $L\alpha$, Fe $L\alpha$, and O $K\alpha$ spectra revealed that the highest occupied states have mainly a Cu d character, while Fe d and O p states lie deeper in energy. In the same work, the oxidation state of each of the ions has been determined, and the Cu ions were found to be in the Cu^{1+} oxidation state and the Fe^{3+} ions in the high-spin $S = 5/2$ configuration. Subsequently, x-ray absorption experiments have been carried out to characterize the lowest unoccupied states [24]. Inspecting the low-energy absorption edge, the main contribution to the bottom of the conduction band has been attributed to Fe $3d$ and O $2p$ states. Moreover, the O K-edge x-ray absorption spectrum (XAS) reveals partial $3d$ holes on the Cu ions, indicating a not completely filled $3d$ shell ($3d^{10-x}$). The visible absorption edges, investigated with resonant inelastic x-ray scattering (RIXS) spectroscopic measurements, correspond to Cu → Fe charge transfer [13].

Recent spectroscopic ellipsometry experiments [13] measured an optical band gap of 1.43 eV, in agreement with a previous indirect estimate, 1.5 eV, based on the analysis of the Mott-Schottky diagram [10]. To the best of our knowledge, a combined photoemission–inverse-photoemission experiment to determine the quasiparticle band gap has not yet been reported.

The first theoretical investigation of CFO in the framework of the density functional theory (DFT) appeared in 1997 [23]. In that work, the authors applied the LSDA($+U$) approach to study the density of states, comparing it with x-ray photoelectron spectra. Subsequent theoretical studies focused on the electronic structure of general Cu-based delafossite compounds [25,26] or specifically on the multiferroicity of CFO [27,28]. PBE $+ U$ and HSE calculations, aimed at supporting optical spectroscopic and PEC measurements, appeared recently in the literature [13,29]. The general idea that emerges from these works is that the bare PBE fails in describing the electronic structure of CFO, and corrections must be introduced in the exchange-correlation functional in the form of on-site Hubbard U or exact Hartree-Fock exchange. In a recent contribution, we evaluated the thermodynamic stability of the CFO delafossite phase in the Cu-Fe-O system, employing *ab initio* thermodynamics techniques using PBE $+ U$ total energies [30].

In the present work, we employed DFT calculations to investigate the electronic structure of CFO, analyzing how different exchange-correlation functionals describe quantities such as the band gap, the position of Fe-, Cu-, and O-derived electronic states, and the crystal-field splitting of the Fe $3d$ states, comparing them with the available spectroscopic measurements. Moreover, we focused on aspects that have not been treated specifically in previous theoretical studies, in particular the origin of the $t_{2g} - e_g$ splitting and how these states are affected by the Hubbard U correction.

Our calculations confirm that the PBE functional alone is not sufficient to describe correctly the electronic structure of CFO, predicting a metallic character. We report the self-consistent procedure to obtain a value of the Hubbard U free from any arbitrary choice, and we show how, at the PBE $+ U$ level, the semiconducting behavior is recovered but some aspects of the electronic structure are still not properly described. For instance, the band gap is underestimated and the crystal-field splitting of the conduction bands is not correctly reproduced. On the other hand, we found that hybrid functionals provide results in excellent agreement with the experiments, albeit at a much higher computational cost, if the fraction of exact exchange is appropriately tuned. The outcomes of this work provide a detailed understanding of the electronic structure of CFO that may serve as a starting point for any future investigations of this material.

II. COMPUTATIONAL METHODS

The calculations of this work have been carried out using the plane-wave-pseudopotential approach implemented in the QUANTUM ESPRESSO (QE) code [31,32], employing optimized norm-conserving Vanderbilt (ONCV) pseudopotentials [33,34] to model the electron-ion interaction. The $3s$ and $3p$ semicore states are explicitly included in the valence set for both Fe and Cu pseudopotentials. We employed the Perdew-Burke-Ernzerhof (PBE) [35] exchange-correlation functional with the Hubbard U corrections (PBE+U), the hybrid PBE0 [36] and Heyd-Scuseria-Ernzerhof (HSE) functionals [37] and the meta-GGA SCAN functional [38]. We applied an energy cutoff for the plane waves of 80 Ry (1088 eV) and a $6 \times 6 \times 6$ Γ-centered $\mathbf{k}$-point sampling of the Brillouin zone (BZ) to converge the total energy per atom within 0.5 mRy (7 meV).

We performed the PBE+U calculations [39–41] within the simplified rotational-invariant approach of Cococcioni and de Gironcoli, computing the value of U with the linear-response method [42]. The hybrid functionals calculations have been performed with a variable fraction α of exact exchange, which has been computed on a $2 \times 2 \times 2$ $\mathbf{q}$-subgrid. For HSE calculations, we adopted the recommended screening parameter $\omega = 0.11\ (\mathrm{a.u.})^{-1}$ [43].

The maximally localized Wannier functions (MLWFs) [44], adopted to investigate the origin of the crystal-field splitting, have been computed using the WANNIER90 code [45], interfaced with the QE software package.

The delafossite structure of CFO, consisting in alternating dumbbell coordinated Cu and octahedral FeO_6 layers [Fig. 1(a)], was modeled using the rhombohedral primitive cell depicted in Fig. 1(b), which belongs to the space group $R\bar{3}m$. This is the structure adopted by CFO at room temperature, while below 16 K this material exhibits structural and magnetic phase transitions, which include a monoclinic unit cell with the $C2/m$ symmetry [46–49]. We considered a collinear, ferromagnetic arrangement of the spins around the Fe ion, since the difference in energy with the antiferromagnetic configurations (32 meV per formula unit) is of the order of the numerical accuracy of the calculation, and the ferromagnetic arrangement has the smallest unit cell.

III. ELECTRONIC STRUCTURE OF BULK CuFeO_2

A. Electronic structure with the PBE functional

The relaxed geometry of CFO computed with the PBE functional is in good agreement with the available experi-

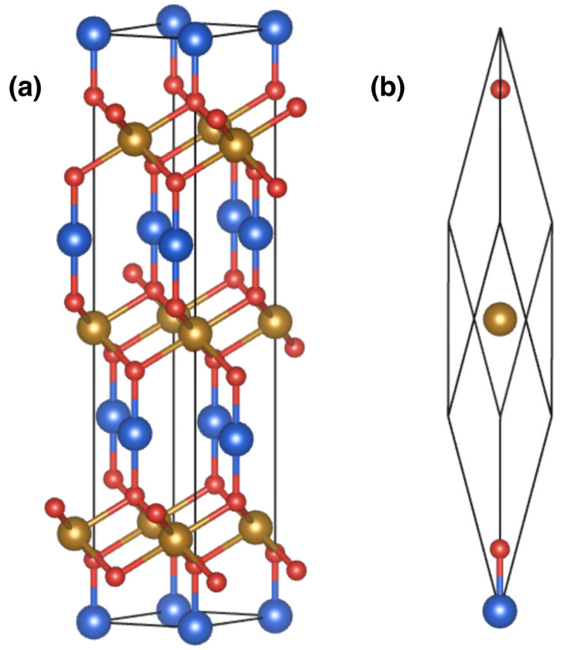

FIG. 1. (a) Crystal structure of $CuFeO_2$ and (b) rhombohedral unit cell. Cu, Fe, and O atoms are represented by blue, yellow, and red spheres, respectively.

mental data, based on neutron diffraction measurements [50]. The experimental lattice constants a and c in the hexagonal unit cell are 3.03 and 17.09 Å, respectively. PBE slightly overestimates these values, giving 3.03 Å (+0.6%) and 17.36 Å (+1.6%).

However, as is commonly the case for transition-metal oxides [42], the PBE functional fails to describe the semiconducting character of CFO. Within this scheme, bulk CFO is wrongly predicted to be a metal, as shown in the spin-polarized projected density of states (PDOS) in Fig. 2, where the Fermi level cuts the tails of the majority- and minority-spin manifolds. We will show in the following sections that the introduction of the on-site Hubbard U on Fe $3d$ states or a fraction of exact exchange are viable methods to open the gap.

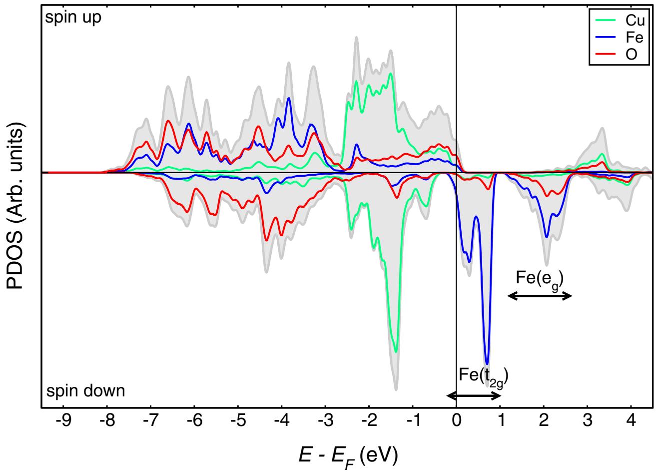

FIG. 2. Spin-polarized projected density of states of $CuFeO_2$, computed with the PBE exchange-correlation functional. The zero of the energy is set to the Fermi energy.

In spite of this failure, the PBE functional correctly predicts the character of the lowest unoccupied states. The first two groups of unoccupied states have a strong Fe d character, while the third group, 3.5 eV above the Fermi level, is dominated by Cu contributions from the $3d_{z^2}$ and $4s$ states, revealing that the $3d$ shell of Cu is not completely filled ($3d^{10-x}$). This observation is consistent with the measured Cu $L_{2,3}$-edge XAS spectrum [24], which established the presence of a partial hole on Cu $3d$ states.

At the PBE level, the Fe ion is correctly predicted to be in the Fe^{3+} high spin ($S = \frac{5}{2}$) state. Note that the oxidation state is calculated following the method of Sit *et al.* [51], where the number of electrons attributed to a certain ion corresponds to the number of eigenvalues of the occupation matrix equal or close to 1. The five eigenvalues of the Fe $3d$ occupation matrix in CFO are close to 1 for one spin channel, while in the other they are significantly smaller (<0.4). Given this configuration, five electrons are formally assigned to the Fe ion, and all of them lie in the majority-spin channel. In Fe^{3+} compounds, a large exchange energy, ∼4.1 eV [52], separates the majority from the minority Fe d orbitals, with the latter lying above the Fermi energy.

In addition, the electrostatic field arising from the octahedral set of surrounding oxygen atoms, seen only as six point charges, breaks the symmetry of the fivefold-degenerate d orbitals of the central Fe ion, splitting the lowest conduction states into the threefold-degenerate t_{2g} and the twofold-degenerate e_g manifolds [53]. Going beyond the pure electrostatic picture, the e_g orbitals, namely d_{z^2} and $d_{x^2-y^2}$, oriented directly toward the ligands, interact with the O p orbitals forming bonding e_g and antibonding e_g^* combinations. The bonding combination has a stronger O character, while the antibonding contains a prevalent Fe component. Conversely, the t_{2g} (d_{xy}, d_{yz}, and d_{zx}), which lie in between two Fe-O bonds, are nonbonding.

According to PBE level PDOS analysis, the t_{2g} and e_g manifolds are separated by 1.5 eV, in good agreement with the experimental energy difference (1.35 eV) measured in the XAS spectrum and attributed to the Fe $3d$–O $2p$ overlap [24]. As we will show in Sec. III B, the introduction of a Hubbard term U on Fe $3d$ electrons has a very significant effect on this splitting. Since CFO operates as a photocathode, a deeper understanding of the character of the conduction band is of critical importance. In the following, we will therefore analyze in detail the physical origin of the energetic splitting of the $t_{2g} - e_g$ states.

The splitting contains contributions from both the Coulomb repulsion and the hybridization between the transition-metal d states with the ligand p states, as previously stated. Following the procedure outlined in Ref. [54], which is based on the on-site energies of MLWFs derived from varying Bloch states, it is possible to distinguish between the two contributions. We focus only on the minority-spin channel, since it gives rise to the conduction-band states whose crystal-field splitting can be directly compared with experimental values. The band structure of the minority-spin channel is reported in Fig. 3. The different colors of the bands not only denote the main character of the states, but they also indicate

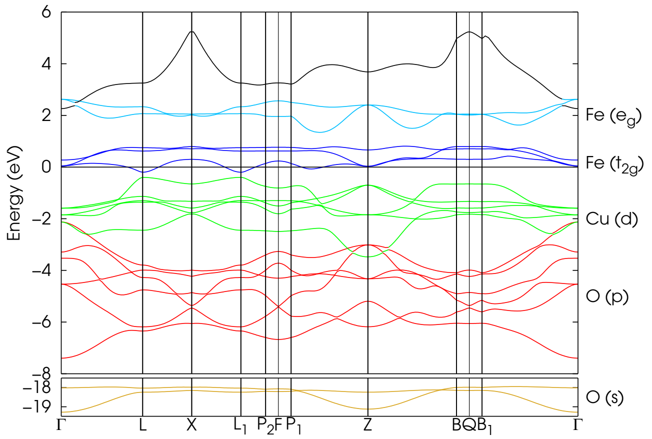

FIG. 3. Minority-spin band structure. The different colors represent the main character of the band, according to the PDOS: O *s* (gold), O *p* (red), Cu *d* (green), Fe t_{2g} (dark blue), Fe e_g (light blue), and Cu *s* (black).

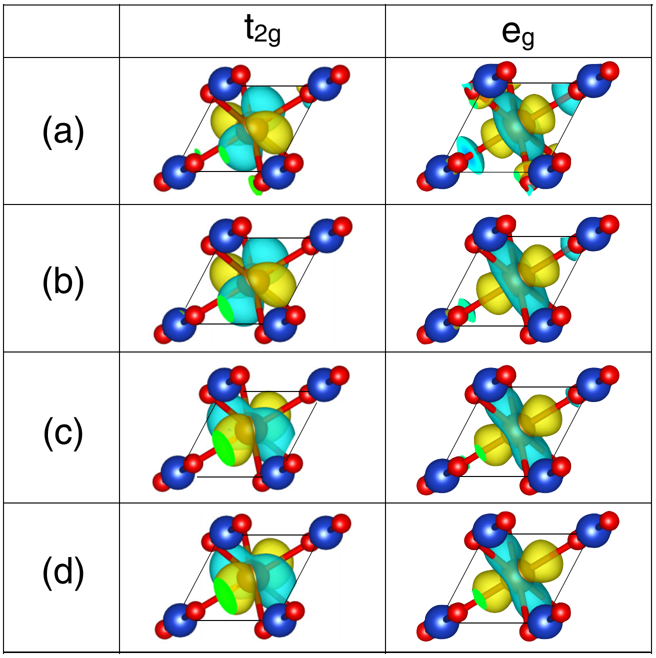

FIG. 4. Representative MLWFs for the t_{2g} and the e_g set inside the unit cell. In the row (a) the bands with t_{2g} (e_g) are included separately in the summation. We then add in the summation the Kohn-Sham states with a prevalent O *p* (b), Cu *d* (c), and O *s* (d) character.

the stage at which the states are included in the summation for the construction of the MLWFs:

$$|w_{n,\mathbf{R}}\rangle = \frac{V}{(2\pi)^3}\int_{\mathrm{BZ}} d\mathbf{k}\, e^{-i\mathbf{k}\cdot\mathbf{R}} \sum_{m=1}^{N} U_{mn}^{(\mathbf{k})} |\psi_{n,\mathbf{k}}\rangle. \tag{1}$$

Here, $|w_{n,\mathbf{R}}\rangle$ denotes the Wannier function characterized by a unit-cell vector $\mathbf{R}$ and a band index n, constructed from a set of N Bloch states $|\psi_{n,\mathbf{k}}\rangle$ via a unitary transformation $\mathbf{U}$ that mixes the Bloch states at a specific $\mathbf{k}$-point. A more detailed description is reported in the Supplemental Material [55], which contains Refs. [56–69].

In the first instance, we construct the MLWFs including in Eq. (1) first the t_{2g} bands (dark blue in Fig. 3) and then, separately, the e_g bands (light blue). It should be noted that, while the group of t_{2g} states is well separated from the other bands, this is not the case for the e_g set, which cross with Cu states at the Γ-point. In the latter case, we adopted the disentanglement procedure introduced by Souza *et al.* [70] to decouple the bands. The plot of one representative MLWF among the three t_{2g} states and one among the e_g is reported in Fig. 4(a).

The resulting MLWFs are centered on the Fe atoms and, while those corresponding to the t_{2g} states assume the shape of atomiclike orbitals, the tails of the e_g states are extended on the surrounding oxygen atoms. The on-site energies for each MLWF are indicated as $\varepsilon^{(d)}$ in the scheme in Fig. 5. The splitting at this stage between the twofold-degenerate e_g states and the threefold-degenerate t_{2g} amounts to 1.55 eV, in agreement with the difference between the peaks in the PDOS.

In the second step, we construct the set of MLWFs including both Fe *d* (dark and light blue in Fig. 3) and O *p* (red) states in the summation. We applied again the disentanglement procedure to treat the crossing between the red and green bands around the Γ and *Z* points. The MLWFs centered on the Fe ions are decoupled from those centered on the oxygen atoms, and the contribution due to $d-p$ hybridization is removed from the on-site energies. The effect is most notably evident on the e_g MLWFs, whose tail on the surrounding oxygen atoms is significantly reduced, as shown in Fig. 4(b). The corresponding on-site energy, indicated as $\varepsilon^{(dp)}$, is reduced by 1.00 eV, while for the t_{2g} the difference is only 0.24 eV, indicating the different degrees of hybridization between the Fe *d* states with the ligands. Moreover, the explicit inclusion of the Kohn-Sham states with O *p* character in the summation breaks the symmetry of the threefold-degenerate t_{2g} manifold, with one state lying 16 meV higher than the other two. This effect is due to the rhombohedral arrangement of the oxygen atoms around the central iron,

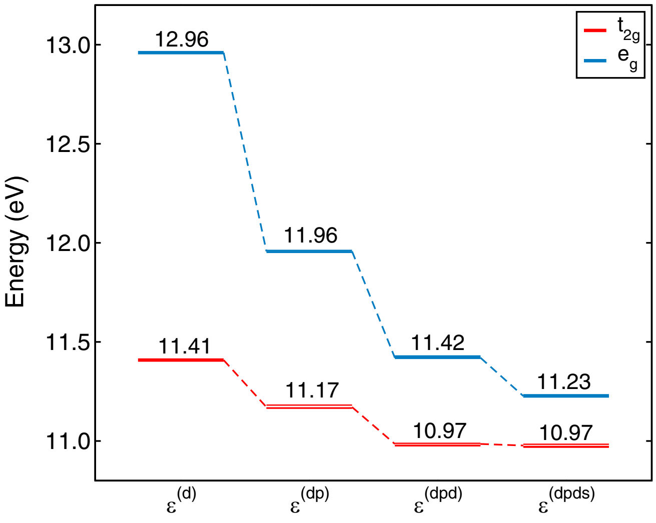

FIG. 5. On-site energies of the MLWFs corresponding to the $t_{2g}-e_g$ states, obtained including different sets of Kohn-Sham states in the summation in Eq. (1).

which differs slightly from the octahedral configuration. In a rhombohedral environment, the t_{2g} states are split into two subgroups, one with the a_{1g} representation, which corresponds to the linear combination $|a_{1g}\rangle = \frac{1}{\sqrt{3}}(|xy\rangle + |yz\rangle + |zx\rangle)$, and the other with the two-dimensional e_g representation, containing the linear combinations $|e_g^1\rangle = \frac{1}{\sqrt{6}}(2|xy\rangle - |yz\rangle - |zx\rangle)$ and $|e_g^2\rangle = \frac{1}{\sqrt{2}}(|yz\rangle - |zx\rangle)$ [71].

To remove possible hybridization effects associated with Cu d states, we include them (green bands in Fig. 3) in the summation and compute the corresponding on-site energies, $\varepsilon^{(dpd)}$. The on-site energy corresponding to the e_g orbitals is further reduced by 0.55 eV, while only 0.20 eV is removed from the t_{2g} on-site energy obtained at the previous stage. Yet, this comparably small change in energy is accompanied by a change in the shape of the t_{2g} orbitals, which resemble the rhombohedral a_{1g} and e_g orbitals, as shown in Fig. 4(c).

Finally, we include the O s states, depicted in gold in Fig. 3, in the summation. These lie around 18.5 eV below the Fermi level. The t_{2g} are unaffected by the inclusion of these states while a small contribution of 0.19 eV is removed from the e_g on-site energies, indicating that a small Fe e_g–O s mixture was still present in the MLWFs. The difference between the e_g and the t_{2g} on-site energies obtained at this level, $\varepsilon^{(dpds)}$, amounts to 0.26 eV and can be interpreted as the pure electrostatic contribution to the crystal-field splitting [54]. The remaining 1.29 eV instead can be thought of as a consequence of the hybridization between the d states and the O p, O s, and Cu p atomic orbitals. This hybridization effect is more pronounced in e_g, which experiences a larger shift when further states are added to the summation in Eq. (1).

B. Electronic structure with the PBE + U functional

Although our PBE simulations reproduce some experimental results, in order to recover the semiconducting character of CFO we explored the effect of adding a Hubbard U correction to the exchange correlation functional, which acts specifically on the d states. The treatment of the strongly correlated Fe ions in CFO by the Hubbard U approach is seriously conflicted within the available literature. Even though the appropriate value of U to apply depends on the set of pseudopotentials and the adopted projection methods, and therefore is not necessarily comparable across different computational approaches, there is a large diversity in the Hubbard U corrections applied to the Fe^{3+} ions in CFO reported in the literature [23,25,26,28]. Values of the effective Hubbard parameter range from 2.2 to 7.1 eV, and in one case the Hubbard term is applied also to Cu^{1+} ions [23]. In this work, the correction is only applied to Fe ions, which are the main source of the metallic behavior. Furthermore, it has previously been shown that the U correction does not improve the description of the electronic structure of Cu^{1+} compounds, where the d shell is completely filled, for instance in the case of Cu_2O [5].

To compute the Hubbard U correction for our computational setup, we followed the linear-response formulation of Cococcioni and de Gironcoli [42], adapted to include the self-consistency procedure introduced by Kulik *et al.* [72]. In addition, we performed an extra geometry self-consistency cycle in order to capture any changes to the U correction associated with the rehybridization of the orbitals due to changes in the nuclear coordinates.

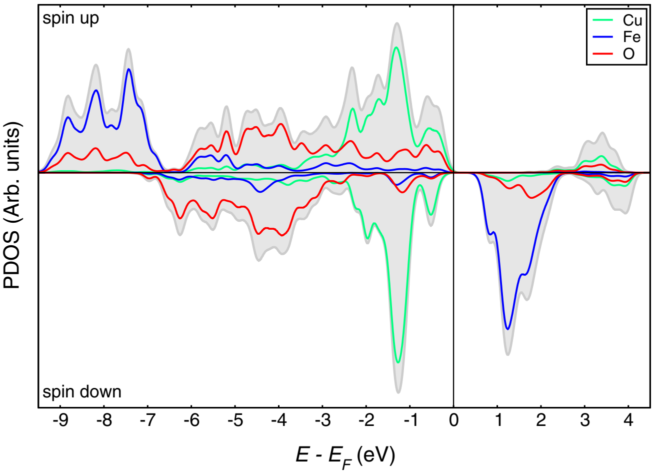

FIG. 6. Projected density of states at the PBE + U level, computed with the self-consistent value of U.

The linear-response procedure [55] reveals U_{scf} to be converged within 50 meV to a value of 4.1 eV. This value is in line with other DFT+U studies of Fe^{3+}-based oxides, in which U was not computed via linear-response calculations, but it was tuned to 4.2 and 4.0 eV in order to obtain the experimental energy gap [73] and the formation enthalpy [74] of $\alpha - Fe_2O_3$, respectively. A similar value, $U = 4.3$ eV, has also been evaluated for $\alpha - Fe_2O_3$ following an *ab initio* approach based on unrestricted Hartree-Fock theory [75].

The optimized equilibrium lattice constants a and c, in the hexagonal description, are 3.10 Å (+2.3% with respect to the experimental value) and 17.32 Å (+1, 3%), respectively, resulting in a very similar geometry compared to that obtained with the PBE functional.

The PDOS at the PBE+U_{scf} level is reported in Fig. 6. The computed band gap, which is still lower than the experimentally measured value, is 0.80 eV. In addition to underestimating the band gap, we find that the conduction-band states are also altered by the Hubbard U: the splitting between the unoccupied Fe t_{2g} and e_g states is not preserved when the U correction is added, and the two manifolds collapse in a single peak in the PDOS. This outcome is in disagreement with the experimental XAS measurements, where the two peaks are easily distinguishable and separated by a gap of 1.35 eV [24].

A similar behavior in CFO has been reported in the supporting information of Ref. [13]. However, this effect is not peculiar to this compound, but it has been shown that it occurs when DFT + U is applied to other Fe^{3+} compounds such as hematite [76] and $BiFeO_3$ [77]. Interestingly, Cr^{3+} in CrI_3 displays a similar behavior [78].

Determining the origin of this result is important in assessing the application of the DFT+U to CFO, since an accurate description of the empty conduction-band states is of paramount importance for understanding the ability to act as the photocathode. To explain the origin of this failure, we note that, in a first approximation, neglecting effects due to charge rearrangement, the Kohn-Sham eigenvalues $\epsilon_{\mathbf{k}v}^{\sigma}$ are

TABLE I. Occupation numbers of the minority-spin Fe d orbitals in CFO at the PBE level and projection of the t_{2g} and e_g states at the Γ point onto the atomic orbitals. The last column represents the shift produced by the $U = 4.1$ eV on these states computed using Eq. (2).

	d_{xy}	d_{zx}	d_{zy}	d_{z^2}	$d_{x^2-y^2}$	$\Delta\epsilon_{n\mathbf{k}}^{U=4.1}$ (eV)
$n_{I,m}^{\downarrow}$	**0.197**	**0.199**	**0.202**	**0.376**	**0.376**	
$\lvert\langle\phi_m^I\lvert\psi^{\downarrow}_{\Gamma t^1_{2g}}\rangle\rvert^2$	0.279	0.522	0.003	0.002	0.181	**+1.08**
$\lvert\langle\phi_m^I\lvert\psi^{\downarrow}_{\Gamma t^2_{2g}}\rangle\rvert^2$	0.300	0.103	0.505	0.078	0.000	**+1.16**
$\lvert\langle\phi_m^I\lvert\psi^{\downarrow}_{\Gamma t^3_{2g}}\rangle\rvert^2$	0.266	0.213	0.325	0.008	0.004	**+1.00**
$\lvert\langle\phi_m^I\lvert\psi^{\downarrow}_{\Gamma e^1_{g}}\rangle\rvert^2$	0.035	0.047	0.008	0.003	0.501	**+0.37**
$\lvert\langle\phi_m^I\lvert\psi^{\downarrow}_{\Gamma e^2_{g}}\rangle\rvert^2$	0.003	0.001	0.032	0.555	0.005	**+0.33**

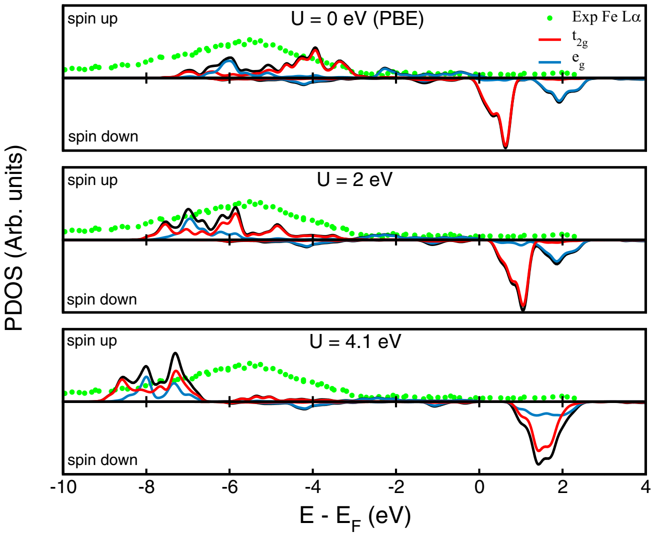

FIG. 7. Projected density of states onto the Fe t_{2g} (red line) and e_g (green line) d states for different values of the applied Hubbard U. The green dots represent the experimental data of Fe $L\alpha$ edge x-ray emission spectrum, taken from Ref. [23].

rigidly shifted by the Hubbard U according to the following equation [55]:

$$\begin{aligned}\epsilon_{\mathbf{k}v}^{\sigma\,\mathrm{DFT}+U} &= \epsilon_{\mathbf{k}v}^{\sigma\,\mathrm{DFT}} + \langle\psi_{\mathbf{k}v}^{\sigma}\lvert V_U\rvert\psi_{\mathbf{k}v}^{\sigma}\rangle \\ &= \epsilon_{\mathbf{k}v}^{\sigma\,\mathrm{DFT}} + U\sum_{I,m}\left(\frac{1}{2} - n_m^{I,\sigma}\right)\lvert\langle\phi_m^I\lvert\psi_{\mathbf{k}v}^{\sigma}\rangle\rvert^2. \end{aligned} \tag{2}$$

The value of the shift depends on the occupation numbers $n_{m,\sigma}^I$ of the corresponding d orbitals and on the projection of the Kohn-Sham states onto the atomic Fe d orbitals. The occupation numbers $n_{m,\sigma}^I$ in the minority-spin channel of the d states of Fe obtained with the PBE functional are reported in the first row of Table I.

On the basis of the Fe^{3+} oxidation state and the high-spin character, it could be naively expected that the occupation numbers $n_{m,\sigma}^I$ would be zero. However, the occupation numbers can assume values greater than 0 due to hybridization and projection effects. It has been shown that when a transition metal and a ligand form a covalent bond, if only the bonding state is occupied, a projection procedure onto the d orbitals could give rise to occupation numbers greater than 0, whose origin resides only in the orbital mixing [51]. As already pointed out, the d_{z^2} and $d_{x^2-y^2}$ orbitals hybridize with the p orbitals of the ligands, forming σ bonding and antibonding combinations, and the projection of the occupied bonding Kohn-Sham states with a prevalent O character, but a smaller Fe contribution, onto the atomic d_{z^2} and $d_{x^2-y^2}$ orbitals gives rise to nonzero occupation numbers. The atomic d_{xy}, d_{zx}, and d_{zy} orbitals are not formally hybridized with the oxygen orbitals in a pure tight-binding picture. However, the tail of the atomic projectors can give rise to spurious interactions that could enhance the value of the occupation number. The results of DFT + U calculations depend considerably on the choice of the local projector. The atomic orbitals used in atomiclike projectors have in general a large effective radius, and therefore a larger number of electrons can be accommodated in the d shell [79]. We have shown with the MLWFs analysis that a small hybridization contribution, 0.44 eV, is present in the on-site energies of the t_{2g} states, much smaller than the one in e_g states, 1.73 eV. This different hybridization is reflected in the occupations of d_{z^2} and $d_{x^2-y^2}$, which are larger than those of the other three d orbitals, and, consequently, the corresponding factor ($\frac{1}{2} - n_m^{I,\sigma}$) in Eq. (2) will be smaller.

Moreover, we report in the lower part of Table I the projection of the t_{2g} and e_g Kohn-Sham states at the Γ point onto the five d orbitals. The sum of the projections of the t_{2g} states is close to unity, while it is around 0.6 for e_g, indicating that there is a larger Fe character in the former, as evident also from the PDOS in Fig. 2. The correction on the eigenvalues at the Γ point, computed using Eq. (2) with the self-consistent value of $U = 4.1$ eV, is reported in the last column of Table I. The combination between the different occupation numbers and atomic projections makes the shifts on the t_{2g} states three times bigger than those applied to the e_g with the effect of pushing the former toward the latter and closing the gap between the two manifolds.

The shifts reported in Table I are computed using Eq. (2), in which the PBE wave functions are assumed to be fixed and the potential due to the Hubbard U is applied in a perturbative way. These results are consistent with the eigenvalues reported at the first iteration of the self-consistent cycle, when U is switched on. However, the wave functions are continuously updated during the self-consistent cycle, causing modifications also in the Kohn-Sham potential, and the difference between the corrections applied to the t_{2g} and the e_g states at the end of the cycle is even bigger than the prediction made with Eq. (2), with the consequence of further reducing the gap.

In Fig. 7, we compare the PDOS on the Fe atomic orbitals for three different values of U with the experimental Fe $L\alpha$ x-ray emission spectrum. The occupied majority-spin states shift rigidly with U toward lower energies as expected by the fact that their occupation number is close to 1. A comparison with the experimental data reveals that the position of the occupied Fe d state is well reproduced for small values of the Hubbard U, while they are pushed toward lower energies when the self-consistent value is employed. The unoccupied minority-spin t_{2g} states are shifted linearly with U toward the

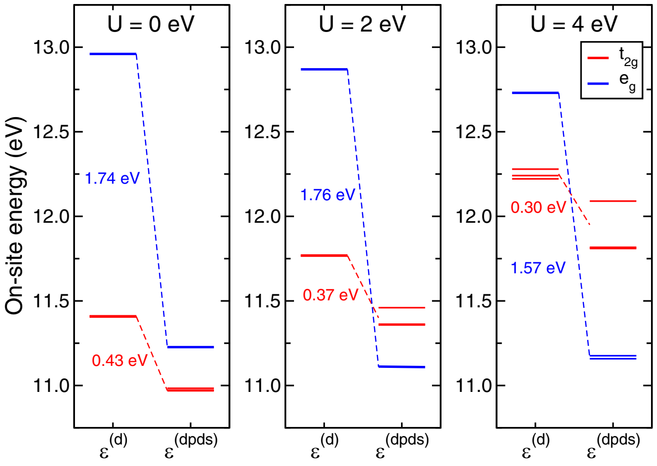

FIG. 8. On-site energies of the MLWFs corresponding to the t_{2g} and e_g states for three different values of the Hubbard U.

e_g states, which are almost unaltered. The two manifolds start overlapping for $U = 2$ eV and they collapse into a single peak when the self-consistent value of U (4.1 eV) is applied.

As pointed out above, the magnitude of the shift experienced by the t_{2g} and e_g states when U is applied depends on the different degrees of hybridization that those states have with the orbitals of the surrounding atoms. To investigate the effect of U on the hybridization of Fe d with the other orbitals, we analyzed MLWFs constructed from different DFT + U wave functions and eigenvalues. More explicitly, for each value of U considered, we built MLWFs including in the first instance only the t_{2g} and e_g states, and then including the O p, Cu d, and O s states within the summation [see Eq. (1)]. We noted in Sec. III A that the difference between the on-site energies of the MLWFs $\epsilon^{(d)} - \epsilon^{(dpds)}$ can be interpreted as a working definition of hybridization effects on a particular orbital.

We plot schematically the on-site energies of the MLWFs for three different values of U in Fig. 8. The on-site energy, $\epsilon^{(d)}$, of the MLWFs relative to the t_{2g} states gets closer to the e_g state as U increases, reflecting the collapse of the two manifolds in the PDOS in Fig. 7.

The spurious effect that the introduction of the Hubbard correction has on the two manifolds becomes clear once we decompose the crystal-field splitting in electrostatic and hybridization effects. The difference between the on-site energies $\epsilon^{(d)}$ and $\epsilon^{(dpds)}$ of the MLWF corresponding to the e_g states changes from 1.74 eV for $U = 0$ eV to 1.57 eV for $U = 4$ eV, indicating that the impact of U in reducing the hybridization is fairly small, −0.2 eV. Similarly, for the t_{2g} states the change in hybridization due to U modifies the difference between $\epsilon^{(d)}$ and $\epsilon^{(dpds)}$ from 0.43 to 0.30 eV.

When we set $U = 2$ eV, the on-site energy $\epsilon^{(dpds)}$ of the e_g states becomes smaller than that of the t_{2g}, and this effect is further amplified for $U = 4$ eV, in which the e_g states lie 0.8 eV lower than the t_{2g}. The reverse ordering of these states would correspond to an unphysical negative electrostatic crystal-field splitting, in contrast with the pure electrostatic picture [53]. This inversion suggests that the interpretation of the difference between the on-site energies as a measure of electrostatic effects is only valid as long as the states are not altered by the introduction of the U correction. The incorrect description of the t_{2g} and e_g states at the DFT + U level affects the on-site energies $\epsilon^{(d)}$ of the MWLFs. These bad starting energies lead to the spurious negative electrostatic crystal-field splitting when hybridization effects, which are weakly dependent on U, are gradually removed passing from $\epsilon^{(d)}$ to $\epsilon^{(dpds)}$.

Another spurious effect that arises due to the presence of the Hubbard correction relates to the splitting of the t_{2g} states into the a_{1g} and e_g subgroups due to the rhombohedral arrangement of atoms. This separation is emphasized with increasing values of U, for example it is most strongly amplified in the case of $U = 4$ eV, where it is equal to 0.25 eV.

Overall, some aspects of the electronic structure of bulk CFO improve when a Hubbard U term is applied to Fe $3d$ states. In particular, this approach recovers the semiconducting character of the material, which is fundamental for PEC applications. Even though the gap is underestimated, the conduction band is correctly predicted to have Fe $3d$ character, and the valence band is mostly Cu $3d$, in agreement with photoemission experiments [23,24]. The drawback in this approach resides in the fact that the splitting of the Fe $3d$ $t_{2g} - e_g$ levels in the conduction band disappears using the self-consistent value of U. It is worthwhile to note that potential solutions to this issue have already been proposed, based either on a separate treatment of the t_{2g} and e_g electrons in DFT + U [80], or using a suborbital dependent U [81]. Alternatively, the application of an intrasite correction V [82] could favor the decoupling of the e_g states from the O p orbitals, favoring the shift applied by U. However, if the total energies are properly corrected, PBE + U has proved to be a good starting point in describing the formation energies of CFO and other compound Cu-Fe based compounds [30].

C. Hybrid and meta-GGA functionals

An alternative approach to address the shortcomings of the PBE functional in reproducing the semiconducting character of CFO is to include a fraction of exact Hartree-Fock exchange within the exchange-correlation functional. To this end, we employ the hybrid functionals PBE0 and HSE, on top of the PBE and PBE + U optimized geometry, tuning the fraction α of the exact exchange to reproduce several experimental quantities related to the electronic structure of CFO, in particular the band gap, the crystal-field splitting of the unoccupied Fe $3d$ states, and the position of the Fe $3d$ states in the occupied states. The choice of the starting geometry does not affect the electronic structure significantly, and in the following we report only the electronic structures obtained on top of the PBE + U geometry.

The PDOS for three selected values of the fraction α is reported in Fig. 9. The two functionals provide an equivalent description of the occupied states when the same fraction of exact exchange is applied. A small fraction of exact exchange, around 0.15, is required to describe correctly the position of the occupied Fe d states, compared with the experimental $L\alpha$ edge emission spectrum, as indicated by the dashed lines in Fig. 9. The Fe manifold shifts linearly toward lower energies for increasing α, while the Cu and the O manifolds are only slightly affected and their position is almost constant.

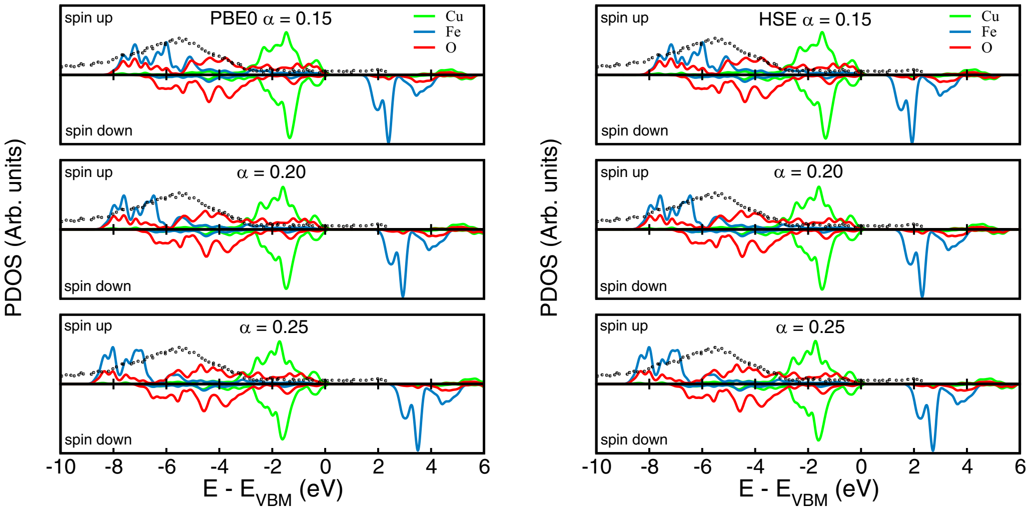

(a) (b)

FIG. 9. Projected density of states for different values of the fraction of exact exchange, using the PBE0 (a) and the HSE hybrid functionals (b). The blue dashed line represents the experimental data of Fe $L\alpha$ edge x-ray emission spectrum, taken from Ref. [23].

The linear shift is applied also to the empty states which move rigidly toward higher energies for increasing α. The t_{2g} and e_g manifolds are well separated for all values of α, and the crystal-field splitting, computed via a weighted average on the PDOS, is plotted in the lower panel of Fig. 10. In the range of α considered, the crystal-field splitting lies within ±0.1 eV of the experimental value, without any indication of the collapse toward a single peak observed at the PBE + U_{scf} level of theory.

In the upper panel of Fig. 10, we report the value of the band gap, comparing it with the optical band gap of 1.43 eV [13]. It should be noted that this comparison is not formally justified, since the optical band gap is renormalized by excitonic effects. Yet, in the absence of an experimental value for the true quasiparticle gap, the optical gap can serve as a rough benchmark. The PBE0 functional predicts a higher band gap than the HSE at the same α, an effect that has been previously observed for Cu_2O [5]. When the standard fraction of exact exchange, 0.25, is employed, the band gap is overestimated by both functionals, indicating that a lower fraction is required to reproduce the optical value. Specifically, HSE requires a fraction of 0.20 to reproduce the experimental optical gap, while a value of $\alpha = 0.14$ is obtained by interpolating the PBE0 data. In both cases, the crystal-field splitting lies within 0.03 eV from the experimental value, while the occupied Fe d states are better reproduced with a low fraction of exact exchange, and so, in this sense, the PBE0 functional may be preferable.

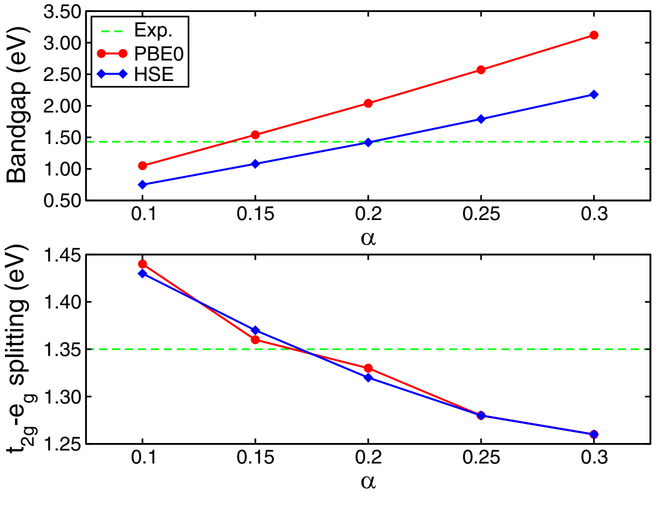

FIG. 10. Band gap (upper panel) and crystal-field splitting (lower panel) in CFO, computed with hybrid functionals using a variable fraction of exact exchange.

There are solid theoretical foundations for which an optimal value for α is given by the reciprocal of the static dielectric constant $\alpha = 1/\epsilon_\infty$ [83,84]. We computed $\epsilon_\infty = \frac{1}{3}\,\text{Tr}[\epsilon]$, where ϵ is the dielectric tensor, computed at the PBE + U level within density functional perturbation theory [85], and we obtained $\alpha = 0.11$. Therefore, it is not surprising that the fraction of exact exchange that provides a band gap in excellent agreement with the experiments is $\alpha = 0.14$, very close to the estimate obtained from $\alpha = 1/\epsilon_\infty$.

Finally, we investigated the structural and electronic properties of CFO using the meta-GGA functional SCAN [38], which was recently shown to provide accurate results for geometries and energies of a vast class of materials [86]. The SCAN lattice constant $a = 3.02$ and $c = 17.24$ Å are closer to their experimental counterparts than those computed at the PBE and the PBE+U level, with an error of −1% for a and +0.88% for c. The PDOS computed at the equilibrium geometry is reported in Fig. 11. While the crystal-field splitting is captured correctly, we obtained a band gap of 0.56 eV. This is a clear improvement over the metallic PBE solution, but is still significantly smaller than the 1.43 eV experimental gap.

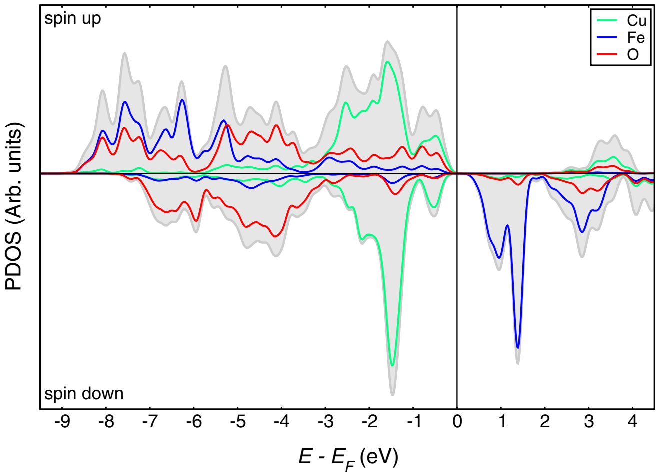

FIG. 11. Projected density of states computed using the meta-GGA SCAN functional.

IV. CONCLUSIONS

In summary, we performed a characterization of the electronic structure of CFO using the DFT formalism, and we presented the pros and cons of the adopted exchange-correlation functionals. First, we have verified the well-known failure of PBE in reproducing the semiconducting character of CFO, whereas the peak of the occupied d states and the crystal-field splitting between the lowest conduction bands with the Fe d character are correctly described. In particular, we analyzed the origin of the crystal-field splitting and we separated the dominant hybridization contribution from the pure electrostatic one, computing the on-site energies of different sets of MLWFs.

We added the Hubbard U correction in the exchange-correlation functional, computing the self-consistent value using the linear-response approach, in order to remove any arbitrariness in the choice of the parameter. This term acts specifically on Fe d states, giving a penalty to delocalized states and favoring the opening of a gap in the band structure. However, the t_{2g} and e_g states behave differently when the correction is applied, due to the different hybridization that those states have with the surrounding oxygen orbitals, and they collapse in a single peak in the PDOS. This represents one of the drawbacks of the DFT + U approach in describing the electronic structure of CFO, in conjunction with the underestimation of the energy gap.

Finally, we employed the PBE0 and the HSE hybrid functional and we tuned the fraction of exact exchange in a range that goes from 0.1 to 0.3. We found that the HSE functional reproduces the experimental band gap when $\alpha = 0.2$, while a lower fraction, 0.14, is required for PBE0. This last value is formally justified by a comparison with the optimal fraction of exact exchange, which corresponds to the reciprocal of the dielectric constant.

ACKNOWLEDGMENTS

We acknowledge the CINECA award under the ISCRA initiative, for the availability of high performance computing resources and support. Most of the calculations of this work were performed on Marconi KNL, under the ISCRA B project named PHOTOSOL.

---

[1] M. G. Walter, E. L. Warren, J. R. McKone, S. W. Boettcher, Q. Mi, E. A. Santori, and N. S. Lewis, Chem. Rev. **110**, 6446 (2010).
[2] K. Sivula and R. van de Krol, Nat. Rev. Mater. **1**, 15010 (2016).
[3] M. Hara, T. Kondo, M. Komoda, S. Ikeda, J. N. Kondo, K. Domen, M. Hara, K. Shinohara, and A. Tanaka, Chem. Commun. 357 (1998).
[4] P. E. de Jongh, D. Vanmaekelbergh, and J. J. Kelly, Chem. Commun. 1069 (1999).
[5] L. Y. Isseroff and E. A. Carter, Phys. Rev. B **85**, 235142 (2012).
[6] A. Paracchino, V. Laporte, K. Sivula, M. Grætzel, and E. Thimsen, Nat. Mater. **10**, 456 (2011).
[7] C. G. Read, Y. Park, and K.-S. Choi, J. Phys. Chem. Lett. **3**, 1872 (2012).
[8] J. Gu, Y. Yan, J. W. Krizan, Q. D. Gibson, Z. M. Detweiler, R. J. Cava, and A. B. Bocarsly, J. Am. Chem. Soc. **136**, 830 (2014).
[9] I. Sullivan, B. Zoellner, and P. A. Maggard, Chem. Mater. **28**, 5999 (2016).
[10] M. S. Prevot, N. Guijarro, and K. Sivula, ChemSusChem **8**, 1359 (2015).
[11] M. S. Prevot, Y. Li, N. Guijarro, and K. Sivula, J. Mater. Chem. A **4**, 3018 (2016).
[12] M. S. Prevot, X. A. Jeanbourquin, W. S. Bouree, F. Abdi, D. Friedrich, R. van de Krol, N. Guijarro, F. Le Formal, and K. Sivula, Chem. Mater. **29**, 4952 (2017).
[13] C.-M. Jiang, S. E. Reyes-Lillo, Y. Liang, Y.-S. Liu, G. Liu, F. M. Toma, D. Prendergast, I. D. Sharp, and J. K. Cooper, Chem. Mater. **31**, 2524 (2019).
[14] A. Muir and H. Wiedersich, J. Phys. Chem. Solids **28**, 65 (1967).
[15] M. Mekata, N. Yaguchi, T. Takagi, S. Mitsuda, and H. Yoshizawa, J. Magn. Magn. Mater. **104–107**, 823 (1992).
[16] T.-R. Zhao, M. Hasegawa, and H. Takei, J. Cryst. Growth **166**, 408 (1996).
[17] S. Mitsuda, N. Kasahara, T. Uno, and M. Mase, J. Phys. Soc. Jpn. **67**, 4026 (1998).
[18] F. Benko and F. Koffyberg, J. Phys. Chem. Solids **48**, 431 (1987).
[19] T. Joshi, T. R. Senty, R. Trappen, J. Zhou, S. Chen, P. Ferrari, P. Borisov, X. Song, M. B. Holcomb, A. D. Bristow, A. L. Cabrera, and D. Lederman, J. Appl. Phys. **117**, 013908 (2015).
[20] Y. Oh, W. Yang, J. Tan, H. Lee, J. Park, and J. Moon, Nanoscale **10**, 3720 (2018).
[21] A. Bera, K. Deb, K. Chattopadhyay, R. Thapa, and B. Saha, Microelectron. Eng. **162**, 23 (2016).
[22] T. Jiang, Y. Zhao, and H. Xue, J. Mater. Sci. **54**, 11951 (2019).
[23] V. R. Galakhov, A. I. Poteryaev, E. Z. Kurmaev, V. I. Anisimov, S. Bartkowski, M. Neumann, Z. W. Lu, B. M. Klein, and T.-R. Zhao, Phys. Rev. B **56**, 4584 (1997).

[24] M. Malvestuto, F. Bondino, E. Magnano, T. T. A. Lummen, P. H. M. van Loosdrecht, and F. Parmigiani, Phys. Rev. B **83**, 134422 (2011).
[25] K. P. Ong, K. Bai, P. Blaha, and P. Wu, Chem. Mater. **19**, 634 (2007).
[26] H. Hiraga, T. Makino, T. Fukumura, H. Weng, and M. Kawasaki, Phys. Rev. B **84**, 041411(R) (2011).
[27] V. Eyert, R. Frésard, and A. Maignan, Phys. Rev. B **78**, 052402 (2008).
[28] Y. Zhang, E. Kan, and M. H. Whangbo, Chem. Mater. **23**, 4181 (2011).
[29] J. Husek, A. Cirri, S. Biswas, A. Asthagiri, and L. R. Baker, J. Phys. Chem. C **122**, 11300 (2018).
[30] M. Ferri, J. Elliott, M. Farnesi Camellone, S. Fabris, and S. Piccinin, J. Phys. Chem. C **123**, 29589 (2019).
[31] P. Giannozzi, S. Baroni, N. Bonini, M. Calandra, R. Car, C. Cavazzoni, D. Ceresoli, G. L. Chiarotti, M. Cococcioni, I. Dabo, A. Dal Corso, S. de Gironcoli, S. Fabris, G. Fratesi, R. Gebauer, U. Gerstmann, C. Gougoussis, A. Kokalj, M. Lazzeri, L. Martin-Samos, N. Marzari, F. Mauri, R. Mazzarello, S. Paolini, A. Pasquarello, L. Paulatto, C. Sbraccia, S. Scandolo, G. Sclauzero, A. P. Seitsonen, A. Smogunov, P. Umari, and R. M. Wentzcovitch, J. Phys.: Condens. Matter **21**, 395502 (2009).
[32] P. Giannozzi, O. Andreussi, T. Brumme, O. Bunau, M. B. Nardelli, M. Calandra, R. Car, C. Cavazzoni, D. Ceresoli, M. Cococcioni, N. Colonna, I. Carnimeo, A. D. Corso, S. de Gironcoli, P. Delugas, R. A. D. Jr, A. Ferretti, A. Floris, G. Fratesi, G. Fugallo, R. Gebauer, U. Gerstmann, F. Giustino, T. Gorni, J. Jia, M. Kawamura, H.-Y. Ko, A. Kokalj, E. Kucukbenli, M. Lazzeri, M. Marsili, N. Marzari, F. Mauri, N. L. Nguyen, H.-V. Nguyen, A. O. de-la Roza, L. Paulatto, S. Ponce, D. Rocca, R. Sabatini, B. Santra, M. Schlipf, A. P. Seitsonen, A. Smogunov, I. Timrov, T. Thonhauser, P. Umari, N. Vast, X. Wu, and S. Baroni, J. Phys.: Condens. Matter **29**, 465901 (2017).
[33] D. R. Hamann, Phys. Rev. B **88**, 085117 (2013).
[34] M. Schlipf and F. Gygi, Comput. Phys. Commun. **196**, 36 (2015).
[35] J. P. Perdew, K. Burke, and M. Ernzerhof, Phys. Rev. Lett. **77**, 3865 (1996).
[36] C. Adamo and V. Barone, J. Chem. Phys. **110**, 6158 (1999).
[37] J. Heyd and G. E. Scuseria, J. Chem. Phys. **120**, 7274 (2004).
[38] J. Sun, A. Ruzsinszky, and J. P. Perdew, Phys. Rev. Lett. **115**, 036402 (2015).
[39] V. I. Anisimov, J. Zaanen, and O. K. Andersen, Phys. Rev. B **44**, 943 (1991).
[40] V. I. Anisimov, I. V. Solovyev, M. A. Korotin, M. T. Czyzyk, and G. A. Sawatzky, Phys. Rev. B **48**, 16929 (1993).
[41] S. L. Dudarev, G. A. Botton, S. Y. Savrasov, C. J. Humphreys, and A. P. Sutton, Phys. Rev. B **57**, 1505 (1998).
[42] M. Cococcioni and S. de Gironcoli, Phys. Rev. B **71**, 035105 (2005).
[43] J. Heyd, G. E. Scuseria, and M. Ernzerhof, J. Chem. Phys. **124**, 219906 (2006).
[44] N. Marzari and D. Vanderbilt, Phys. Rev. B **56**, 12847 (1997).
[45] A. A. Mostofi, J. R. Yates, G. Pizzi, Y.-S. Lee, I. Souza, D. Vanderbilt, and N. Marzari, Comput. Phys. Commun. **185**, 2309 (2014).
[46] S. Mitsuda, H. Yoshizawa, N. Yaguchi, and M. Mekata, J. Phys. Soc. Jpn. **60**, 1885 (1991).
[47] M. Mekata, N. Yaguchi, T. Takagi, T. Sugino, S. Mitsuda, H. Yoshizawa, N. Hosoito, and T. Shinjo, J. Phys. Soc. Jpn. **62**, 4474 (1993).
[48] F. Ye, Y. Ren, Q. Huang, J. A. Fernandez-Baca, P. Dai, J. W. Lynn, and T. Kimura, Phys. Rev. B **73**, 220404(R) (2006).
[49] G. Quirion, M. J. Tagore, M. L. Plumer, and O. A. Petrenko, Phys. Rev. B **77**, 094111 (2008).
[50] R. D. Shannon, D. B. Rogers, and C. T. Prewitt, Inorg. Chem. **10**, 713 (1971).
[51] P. H. Sit, R. Car, M. H. Cohen, and A. Selloni, Inorg. Chem. **50**, 10259 (2011).
[52] D. M. Sherman, Phys. Chem. Miner. **12**, 161 (1985).
[53] D. S. M. Dunn, M. Thomas, and R. G. Pearson, *Some Aspects of Crystal Field Theory* (Harper and Row, New York, 1965).
[54] A. Scaramucci, J. Ammann, N. A. Spaldin, and C. Ederer, J. Phys.: Condens. Matter **27**, 175503 (2015).
[55] See Supplemental Material at http://link.aps.org/supplemental/10.1103/PhysRevB.101.155201 for a detailed description of the methods employed in the main text, in particular DFT+U, hybrid functionals, and maximally localized Wannier functions. A detailed derivation of the self-consistent value of the Hubbard U for CFO is also reported. The supplemental material contains Refs. [56–69].
[56] J. F. Janak, Phys. Rev. B **18**, 7165 (1978).
[57] A. D. Becke, J. Chem. Phys. **98**, 1372 (1993).
[58] S. Kümmel and L. Kronik, Rev. Mod. Phys. **80**, 3 (2008).
[59] K. Kim and K. D. Jordan, J. Phys. Chem. **98**, 10089 (1994).
[60] P. J. Stephens, F. J. Devlin, C. F. Chabalowski, and M. J. Frisch, J. Phys. Chem. **98**, 11623 (1994).
[61] J. P. Perdew, M. Ernzerhof, and K. Burke, J. Chem. Phys. **105**, 9982 (1996).
[62] T. Yanai, D. P. Tew, and N. C. Handy, Chem. Phys. Lett. **393**, 51 (2004).
[63] J. Heyd, G. E. Scuseria, and M. Ernzerhof, J. Chem. Phys. **118**, 8207 (2003).
[64] A. V. Krukau, O. A. Vydrov, A. F. Izmaylov, and G. E. Scuseria, J. Chem. Phys. **125**, 224106 (2006).
[65] A. Alkauskas, P. Broqvist, F. Devynck, and A. Pasquarello, Phys. Rev. Lett. **101**, 106802 (2008).
[66] Z. D. Pozun and G. Henkelman, J. Chem. Phys. **134**, 224706 (2011).
[67] L. Hedin, Phys. Rev. **139**, A796 (1965).
[68] G. H. Wannier, Phys. Rev. **52**, 191 (1937).
[69] D. Pasquier and O. V. Yazyev, 2D Mater. **6**, 025015 (2019).
[70] I. Souza, N. Marzari, and D. Vanderbilt, Phys. Rev. B **65**, 035109 (2001).
[71] Z. Fang, I. V. Solovyev, H. Sawada, and K. Terakura, Phys. Rev. B **59**, 762 (1999).
[72] H. J. Kulik, M. Cococcioni, D. A. Scherlis, and N. Marzari, Phys. Rev. Lett. **97**, 103001 (2006).
[73] M.-T. Nguyen, N. Seriani, S. Piccinin, and R. Gebauer, J. Chem. Phys. **140**, 064703 (2014).
[74] L. Wang, T. Maxisch, and G. Ceder, Phys. Rev. B **73**, 195107 (2006).
[75] N. J. Mosey, P. Liao, and E. A. Carter, J. Chem. Phys. **129**, 014103 (2008).
[76] S. Piccinin, Phys. Chem. Chem. Phys. **21**, 2957 (2019).

[77] J. K. Shenton, D. R. Bowler, and W. L. Cheah, J. Phys.: Condens. Matter **29**, 445501 (2017).

[78] M. Wu, Z. Li, T. Cao, and S. Louie, Nat. Commun. **10**, 2371 (2019).

[79] Y.-C. Wang, Z.-H. Chen, and H. Jiang, J. Chem. Phys. **144**, 144106 (2016).

[80] I. Solovyev, N. Hamada, and K. Terakura, Phys. Rev. B **53**, 7158 (1996).

[81] W. E. Pickett, S. C. Erwin, and E. C. Ethridge, Phys. Rev. B **58**, 1201 (1998).

[82] V. L. Campo, Jr. and M. Cococcioni, J. Phys.: Condens. Matter **22**, 055602 (2010).

[83] A. Alkauskas, P. Broqvist, and A. Pasquarello, Phys. Status Solidi B **248**, 775 (2011).

[84] J. H. Skone, M. Govoni, and G. Galli, Phys. Rev. B **89**, 195112 (2014).

[85] S. Baroni, S. de Gironcoli, A. Dal Corso, and P. Giannozzi, Rev. Mod. Phys. **73**, 515 (2001).

[86] G. Sai Gautam and E. A. Carter, Phys. Rev. Mater. **2**, 095401 (2018).